The impact of interfacial properties on the macroscopic performance of carbon nanotube composites. A FE^2-based multiscale study

Vissarion Papadopoulos, Maria Tavlaki *

National Technical University of Athens, Heroon Polytechniou 9, Zografou GR-15780, Greece

A B S T R A C T

Interfacial shear strength (ISS) is known to significantly affect the mechanical performance of carbon-nanotube (CNT) reinforced composites. To illustrate the combined effect of ISS and CNT weight fraction on the behavior of CNT/polymer, a CNT/polymer cantilever beam was analyzed using a three-level multiscale technique. (1) At the atomic level, a short CNT was modeled with a space-frame structure, using modified molecular structural mechanics (mMSM); this structure was approximated by equivalent beam finite elements at the next level. (2) At the microscopic level, a polymer matrix reinforced with a single CNT was analyzed. (3) At the macroscopic level, a cantilever beam was analyzed concurrently at the micro- and macroscopic level using a nested solution scheme and first-order homogenization. The analyses' results showed that increasing the CNT content can improve the damping properties of the composite structure, if ISS is low enough to achieve an optimum extent of microstructural slippage.

© 2015 Elsevier Ltd. All rights reserved.

1. Introduction

The technological advances of the last decade have spawned a new generation of composite materials, whose production is controlled at the atomic level. One such material is carbon nanotube-reinforced polymer, which consists of carbon nanotubes embedded in a polymer matrix. Carbon nanotubes (CNTs) are essentially a hexagonal grid of carbon atoms, rolled up to form a tube; their molecular structure lends them extraordinary stiffness and strength, ten to one hundred times higher than those of steel, at a fraction of the weight [1].

The interaction between CNTs and the surrounding polymer significantly affects the properties of CNT-reinforced polymer; in general, higher values of shear strength of the CNT-polymer interface result in stronger and stiffer composite material; on the other hand, for lower values of interfacial shear strength (ISS), the amount of energy dissipated due to slippage between the CNT and the polymer is usually higher, improving the damping behavior of the composite [2–7]. The value of ISS varies greatly with the treatment of the surface of CNTs. Pristine CNTs, whose surface is untreated, interact with polymer primarily via van der Waals forces, resulting in low ISS values [8]. However, if functional chains of polymer are introduced on the surface of a CNT via a procedure called functionalization, they can form strong covalent bonds with the surrounding polymer; in this case, ISS values ten times higher than those corresponding to the noncovalent bonding have been documented [8].

Despite extensive research conducted so far [3,8–29], there is currently a paucity of reliable scientific data concerning the mechanisms of stress transfer at the carbon nanotube-polymer interface, which raises questions regarding the constitutive relations of interfacial shear stress. Pullout experiments of multi-walled CNTs (MWCNTs) [24,16] suggested that the pullout process was brittle, rather than ductile for short embedment lengths, which indicated that the CNT-matrix interface failed due to the propagation of a crack along the interface. However, pullout experiments conducted by Ganesan et al. [16] for larger embedment lengths showed the existence of some frictional interaction between the CNT and the matrix after the failure of the CNT-matrix interface. The hypothesis of frictional CNT-polymer interaction is further corroborated by experiments conducted by Kao and Young [11,10], which proved the existence of a hysteresis loop for a single-walled CNT (SWCNT)-reinforced polymer under a cyclic load. Li et al. [30] and Wernik et al.[23] simulated the pullout of pristine MWCNTs from a polymer matrix using a van der Waals potential to describe the CNT-matrix interaction. According to their results, the pullout was ductile and interfacial forces which opposed the pullout force

* Corresponding author.
  E-mail addresses: vpapado@central.ntua.gr (V. Papadopoulos), mariataylaki@hotmail.com (M. Tavlaki).

were applied to a small region at the edge of the CNTs. Chowdhury and Okabe [20] simulated pullout experiments of functionalized CNTs from a polymer matrix and showed, as expected, that bonding between the studied CNTs and polymer was primarily achieved through polymer chains covalently attached to certain carbon atoms of the CNTs. In this case, the bonding forces acted upon discrete points and varied greatly during the pullout, as polymer chains detached from a point on the CNT and reattached to another.

The inconsistencies between the aforementioned physical experiments and numerical simulations highlight the uncertainty surrounding the nature of the interaction between CNTs and other materials. The uncertainty is further exacerbated by the wide inter- and intra- analyst scatter of the relevant experimental data. This is caused in part from the current difficulty of controlling experimental conditions and taking reliable measurements at the atomic scale. The highest value of ISS recorded by Barber et al. [24] measured at around 130 MPa, which is one order of magnitude higher than the values recorded by Ganesan et al. [16] (13 MPa), but much lower than the highest value recorded from numerical simulations [20] (300 MPa). Although the effect of the interface on CNT-reinforced polymer has been studied before (e.g.[2,4,31]), previous analyses were limited to describing the material behavior at the microscopic level; the algorithm developed in this study uses a nested (FE^2) multiscale solution scheme, in order to alleviate the enormous computational effort involved in the analysis of heterogeneous structures. This enables the investigation of the aforementioned effect on virtually any large-scale structure with minimum loss of accuracy.

The introduced multiscale approach is based on a combination of sequential and semi-concurrent (FE^2) methods and bridges multiple length scales, from nano to micro to macro. Due to the previously mentioned difficulty in establishing a rigorous quantification of the interfacial constitutive law, a sensitivity analysis was considered with respect to various values of a so-called ISS parameter, in order to simulate different bonding conditions between the CNTs and the polymer and evaluate their relative influence on the overall structural behavior. More specifically, the analysis was performed on the following three levels: (a) the atomic one, where a lattice of carbon atoms representing a CNT was analyzed as a space frame, (b) the microscopic one, where a representative volume element (RVE) of the carbon-nanotube reinforced polymer was analyzed using finite elements and, finally, (c) the macroscopic one, where a benchmark cantilever-type structure consisting of the polymer was analyzed using again finite elements, as is shown in Fig. 1. For the transition from the atomic to the microscopic level the sequential multiscale technique was applied. On the other hand, in order to minimize the loss of information when transitioning from the microscopic to the macroscopic level, the semi-concurrent multiscale technique was preferred. For the CNT space frame model at the atomic level, the modified molecular structural mechanics approach (mMSM) [32] was used, as it was implemented in Savvas and Papadopoulos [31] and Savvas et al. [2]. For the subsequent level, the behavior of the space frame was approximated by equivalent beam elements (EBEs). At the microscopic level, a single horizontal CNT modeled as an assembly of EBEs was embedded in a poly-ether-ether-ketone (PEEK) matrix and analyzed using the finite element method. A bond slip model [33] was used to describe the CNT-matrix interaction. The microscopic level was linked to the macroscopic one using a first-order homogenization scheme in conjunction with a FE^2 multiscale technique. The numerical experiments conducted showcase the applicability of the proposed multiscale strategy, while useful conclusions have been extracted from a detailed sensitivity analysis with respect to various scenarios of the ISS parameter.
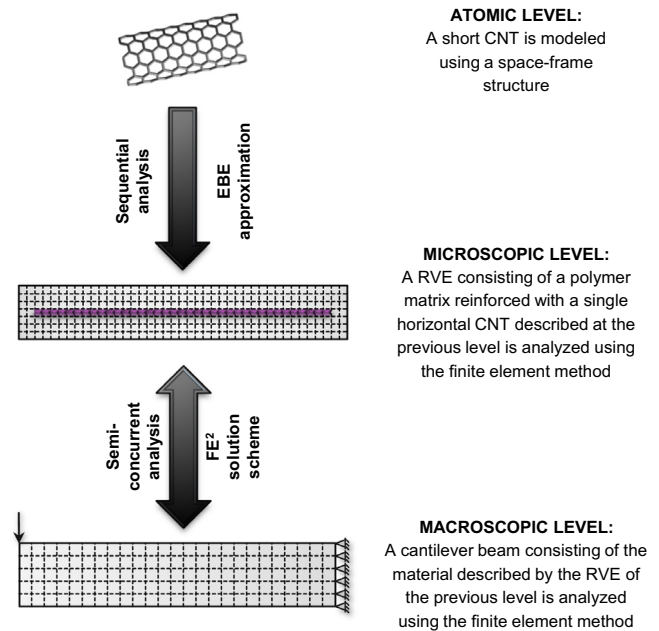

Fig. 1. Overview of the proposed solution.

2. Modeling of carbon nanotubes (atomic level)

2.1. Modified molecular structural mechanics

Carbon nanotubes were modeled using modified molecular structural mechanics (mMSM), according to which the interaction of every carbon atom of the CNT grid is limited to its three nearest neighbors. The covalent bond between each pair of carbon atoms is represented by a rectangular beam element, whose structural properties are such that the change of the potential energy of the beam for every possible displacement of the two atoms is roughly equal to the change of the potential energy of the C—C bond. The C—C bond potential energy is calculated as a function of the bond stretching, bond angle (in-plane) bending, torsion (or dihedral angle torsion) and out of plane bending (or out of plane torsion). Van der Waals interactions are ignored. Analytical relations to calculate the mechanical properties of the beam elements can be found in Savvas et al. [2].

2.2. Transition from the atomic to the microscopic level – the equivalent beam element

The space frame structure by which the CNT is modeled at the atomic level was then projected on an equivalent beam element (EBE), a simplified model much more computationally efficient than the space frame one. The structural properties of the EBEs are calculated by subjecting a cantilever beam to an axial (F_x), transverse (F_y) and a torsional (T) load, as is depicted in Fig. 2. Subsequently the axial stiffness (EA)$_{eq}$, the bending (EI)$_{eq}$ and torsional rigidity (GI)$_{eq}$ are calculated by measuring the horizontal (u_x), vertical displacement (u_y) and the angle of rotation (φ) pertaining to the aforementioned benchmark loads from the following load–deflection relations:

$$(EA)_{eq} = \frac{F_x L_0}{u_x}, \quad (EI)_{eq} = \frac{F_y}{3u_y}L_0^3, \quad (GI)_{eq} = \frac{T}{\phi}L_0 \qquad (1)$$

where L_0 denotes the beam's length.

More information can be found in Savvas et al. [2], who described the EBE approximation.
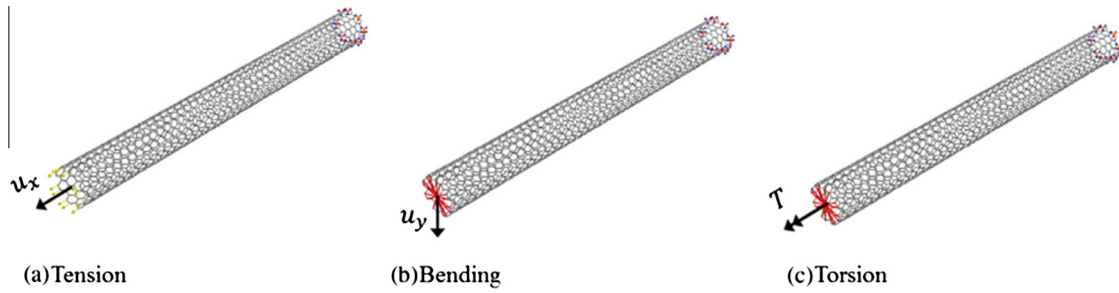
Fig. 2. FE mesh and boundary conditions for (a) Tension, (b) Bending and (c) Torsion loading on CNT model.

3. Modeling at the microscopic level – transition to the macroscopic level (nested solution scheme)

3.1. Homogenization scheme

A homogenization scheme pertaining to linear displacements as was formulated by Miehe and Koch [34] was implemented and applied to the microscopic finite element model of a RVE of polymer matrix and a linear EBE representing the CNT reinforcement inside the matrix (see Fig. 1). According to it, for a given macroscopic strain $\bar{\varepsilon} = [\bar{\varepsilon}_{11}\ \bar{\varepsilon}_{22}\ 2\bar{\varepsilon}_{12}]^T$ a displacement field u is applied to the boundary of the RVE according to the relation:

$$\boldsymbol{u}(\boldsymbol{x}) = \bar{\boldsymbol{\varepsilon}}\boldsymbol{x} \text{ at } \boldsymbol{x} \in \partial\mathcal{V} \tag{2}$$

where $\boldsymbol{x}$ denotes the position vector of a point on the boundary of the RVE and $\partial\mathcal{V}$ denotes the boundary of the RVE. The aforementioned relation constitutes the localization rule, that is, the rule that provides the boundary conditions that are applied on the RVE as a function of a macroscopic variable; in other words, the localization rule is used to transition from the macroscopic to the microscopic level.

After the solution of the boundary value problem resulting from the application of the localization rule, the macroscopic stress $\bar{\boldsymbol{\sigma}} = [\bar{\sigma}_{11}\ \bar{\sigma}_{22}\ \bar{\tau}_{12}]^T$ is calculated as the volume average of the microscopic stress $\boldsymbol{\sigma}$ according to the relation:

$$\bar{\boldsymbol{\sigma}} = \frac{1}{|\mathcal{V}|}sym\left(\int_{\mathcal{V}}\boldsymbol{\sigma}dV\right) \tag{3}$$

where $\mathcal{V}$ denotes the volume of the RVE. Eq. (3) is the homogenization rule, that is, the rule that yields the macroscopic state variables as a function of the microscopic stress state; in other words, the homogenization rule is used to transition from the microscopic level back to the macroscopic one. This transition from the microscopic to the macroscopic and vice versa is schematically depicted in Fig. 3.

Finally, the macroscopic tangent modulus $\bar{\mathbb{C}}$ is calculated as the sensitivity of the macroscopic stress $\bar{\boldsymbol{\sigma}}$ with respect to variations of the macroscopic strain $\bar{\boldsymbol{\varepsilon}}$ according to the relation:

$$\bar{\mathbb{C}} := \partial_{\bar{\boldsymbol{\varepsilon}}}\bar{\boldsymbol{\sigma}} \tag{4}$$

The above equations take a slightly different form if the finite element method is used. In this case, the RVE is appropriately discretized, as shown in Fig. 4. From this point onward, quantities having $\boldsymbol{a}$ as an index refer to internal nodes, whereas quantities having $\boldsymbol{b}$ as an index refer to nodes on the boundary. If we denote the nodal displacement vector with $\boldsymbol{d}$, the localization rule (2) for every node $\boldsymbol{q}$ of the boundary can be written in matrix form as:

$$\boldsymbol{d}_q = \mathbb{D}_q^T\bar{\boldsymbol{\varepsilon}} \tag{5}$$

where $\mathbb{D}_q$ is a matrix that is defined using the nodal coordinates x_1 and x_2 of the node as:

$$\mathbb{D}_q := \frac{1}{2}\begin{bmatrix} 2x_1 & 0 \\ 0 & 2x_2 \\ x_2 & x_1 \end{bmatrix}_q \tag{6}$$

Eq. (5) can be recast in global form as:

$$\boldsymbol{d}_b - \mathbb{D}^T\bar{\boldsymbol{\varepsilon}} = \boldsymbol{0} \tag{7}$$
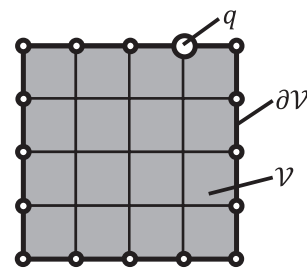

Fig. 4. Schematic representation of a discretized RVE.
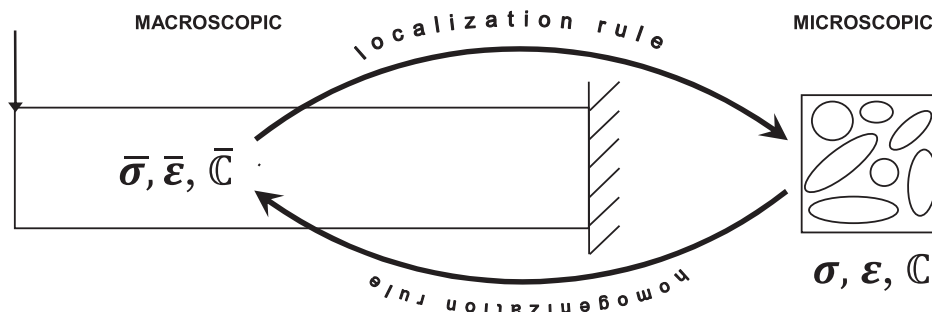

Fig. 3. Overview of the nested solution scheme.

where $[\mathbb{D} := \mathbb{D}_1 \quad \mathbb{D}_2 \quad \ldots \quad \mathbb{D}_M]$ is the global coordinate matrix for all M nodes lying on the boundary.

The equilibrium of the RVE using Lagrange multipliers dictates that:

$$
\begin{aligned}
Q_a(x) &= 0 \\
Q_b(x) - \lambda &= 0 \\
d_b - \mathbb{D}^T \bar{\varepsilon} &= 0
\end{aligned}
\tag{8}
$$

The internal nodal force vector is symbolized with Q and the Lagrange multiplier vector necessary for the enforcement of the boundary conditions with λ. The above set of equations takes the following incremental form for a RVE:

$$
\begin{aligned}
Q_a(x) + K_{aa}\Delta d_a + K_{ab}\Delta d_b &= 0 \\
Q_b(x) - \lambda + K_{ba}\Delta d_a + K_{bb}\Delta d_b - \Delta\lambda &= 0 \\
d_b - \mathbb{D}^T\bar{\varepsilon} + \Delta d_b - \mathbb{D}^T\Delta\bar{\varepsilon} &= 0
\end{aligned}
\tag{9}
$$

where K denotes the tangential stiffness matrix of the RVE.

The solution of the problem is obtained using an iterative Newton–Raphson procedure, as follows: For a given macroscopic stress tensor $\bar{\varepsilon}$ (that is $\Delta d_b = 0$), the nodal displacements d_a are computed iteratively from the first equation according to the relations:

$$
d_a \Leftarrow d_a + \Delta d_a, \quad \Delta d_a = K_{aa}^{-1}Q_a
\tag{10}
$$

The iterations continue until convergence is achieved in the sense that $\|Q_a\| < tol$.

The homogenized macroscopic stress vector is then calculated as:

$$
\bar{\sigma} = \frac{1}{|\mathcal{V}|}\mathbb{D}Q_b
\tag{11}
$$

And the macroscopic tangent modulus as:

$$
\bar{\mathbb{C}} = \frac{1}{|\mathcal{V}|}\mathbb{D}\tilde{K}_{bb}\mathbb{D}^T,
\tag{12}
$$

where the condensed stiffness matrix $\tilde{K}_{bb}$ is equal to:

$$
\tilde{K}_{bb} := K_{bb} - K_{ba}K_{aa}^{-1}K_{ab}
\tag{13}
$$

3.1.1. Polymer-CNT interaction

3.1.1.1. Bond–slip model. The interaction between the polymer matrix and the CNT, which make up the RVE described above, was modeled using a bond–slip mathematical description, as the one proposed by Lykidis and Spiliopoulos [33]. We consider the configuration of Fig. 5, of a fiber embedded in a matrix "parent" element. Assuming that the fiber is only stressed axially, the total displacement of the embedded fiber u_f can be calculated by the superposition of the displacement of the "parent" matrix element
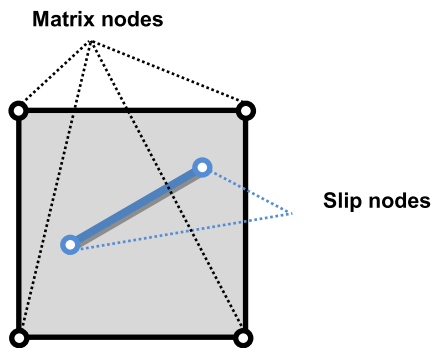

Fig. 5. Schematic representation of a fiber (blue) embedded in a matrix (grey).

u_m along the fiber and the slippage between the two materials s, that is:

$$
u_f = u_m + s
\tag{14}
$$

The matrix displacement along the fiber can be calculated as:

$$
u_m = \{l_1 \ m_1 \ n_1\} \cdot \begin{Bmatrix} u_{m,x} \\ u_{m,y} \\ u_{m,z} \end{Bmatrix}
\tag{15}
$$

where l_1, m_1, n_1 are the directional cosines of the fiber.

Consequently, the strain of the fiber ε_f can be decomposed into a component due to the deformation of the matrix ($\varepsilon_{m,f}$) and a component due to slippage ($\frac{ds}{dl}$):

$$
\varepsilon_f = \frac{du_f}{dl} = \frac{du_m}{dl} + \frac{ds}{dl} = \varepsilon_{m,f} + \frac{ds}{dl}
\tag{16}
$$

The strain of the fiber due to the deformation of the matrix can be calculated as:

$$
\varepsilon_{m,f} = T^* \cdot \varepsilon_m = T^* \cdot B_m \cdot d_m
\tag{17}
$$

Where T^* is calculated from the relation:

$$
T^* = \{l_1^2 \quad m_1^2 \quad n_1^2 \quad l_1 \cdot m_1 \quad m_1 \cdot n_1 \quad l_1 \cdot n_1\}
\tag{18}
$$

We denote with ε_m the strain, with B_m the shape function derivatives and with d_m the nodal displacements of the matrix.

The displacement field of the slip is described using shape functions N_f (assumed to be linear for the current application), and the nodal slippage u_{slip}. Consequently, the strain of the fiber due to slippage is calculated as:

$$
\frac{ds}{dl} = B_f \cdot u_{slip}
\tag{19}
$$

where B_f denotes the shape function derivative of the slip.

Thus, the total strain of the fiber can be expressed in compact form as:

$$
\varepsilon_f = [T^* \cdot B_m \quad B_f] \cdot \begin{Bmatrix} d_m \\ u_{slip} \end{Bmatrix} = B^* \cdot d^*
\tag{20}
$$

The material tangential constitutive relations are assumed to take the form:

$$
\Delta\sigma_m = \mathbb{C}_m \cdot \Delta\varepsilon_m, \quad \Delta\sigma_f = E_f \cdot \Delta\varepsilon_f, \quad \Delta\tau_i = k * \Delta s
\tag{21}
$$

where σ_m denotes the stresses of the matrix, σ_f the axial stress of the fiber and τ_i the interfacial shear stress.

Application of the virtual work theorem yields the following relations for a typical Newton–Raphson iteration between steps t and $t + \Delta t$:

$$
\left\{ \begin{bmatrix} K_{mm} + K_{ff,m} & K_{mf} \\ K_{fm} & K_{ff} + K_{ii} \end{bmatrix} \cdot \begin{Bmatrix} \Delta d_m \\ \Delta u_{slip} \end{Bmatrix} + \begin{Bmatrix} Q_{mf} \\ Q_i \end{Bmatrix} \right\} = \begin{Bmatrix} R_{t+\Delta t} \\ P_{t+\Delta t} \end{Bmatrix}
\tag{22}
$$

The external nodal force vector $[R_{t+\Delta t} \quad P_{t+\Delta t}]^T$ is made up of the external forces $R_{t+\Delta t}$, acting upon the matrix nodes and the forces $P_{t+\Delta t}$, acting upon the slippage nodes (assumed to be zero in this case).

The current internal nodal force vector $[Q_{mf} \quad Q_i]^T$ is calculated as:

$$
\begin{aligned}
Q_{mf} &= \int_{V_m} B_m^T \cdot \sigma_m dV_m + \int_l B_m^T T^{*T} \sigma_f A_f dl \\
Q_i &= \int_l B_f^T \sigma_f A_f dl + Q_s, \quad Q_s = \int_l N_f^T \tau_i O_f dl
\end{aligned}
\tag{23}
$$

We denote with V_m the volume of the matrix, with O_f the fiber section perimeter, with A_f the fiber section area and with l its length.

The elements of the tangential stiffness matrix are calculated as:

$$K_{mm} = \int_{V_m} B_{mT} \cdot C_m \cdot B_m dV_m$$

$$K_{mmf} = \int_l B_{mT} T^{*T} E_f A_f \cdot T^{*T} B_m dl$$

$$K_{mf} = K_{fm}^T = \int_l B_{mT} T^{*T} E_f A_f B_f dl \qquad (24)$$

$$K_{ff} = \int_l B_{fT} E_f A_f B_f dl$$

$$K_{ii} = \int_l N_{fT} k O_f N_f dl$$

3.1.1.2. Constitutive relation of the interfacial shear stress. As mentioned in the introduction, the uncertainty associated with the interfacial constitutive law is large and attributed to multiple sources, both aleatoric and epistemic. This has led the authors to choose a simple ductile model in order to efficiently quantify the uncertainty's impact on the behavior of macroscopic structures and, based on this simplified model, to assess the effect of the interface on the overall structural response. More specifically, CNTs were assumed to interact with the matrix via frictional forces acting upon the whole CNT-matrix interface, which accounted for both covalent and non-covalent bonding. Consequently, a bilinear stick–slip type relation with kinematic hardening was used to describe interfacial shear stress as a function of slippage (see Fig. 8). Values of ISS ranging from zero to infinity were considered, aiming to represent bonding conditions for both pristine and functionalized CNTs. It should be noted at this point that this treatise does not aim to provide an accurate model describing the interface; it merely aims to provide a rough estimate of the upper limit of the damping properties of CNT-reinforced composites (CNT-RCs). This tentative phenomenological model of the CNT-matrix interaction needs to be adjusted as new relevant experimental and analytical data emerge.

3.2. FE² solution scheme

To analyze the macroscopic cantilever beam, the aforementioned homogenization scheme was used within the framework of a semi-concurrent multiscale approach; this particular analysis scheme is also known as a nested or FE² solution scheme, a term coined by Feyel [35]. According to it, the macroscopic model (which consists of a microscopically heterogeneous material) is analyzed concurrently on two separate levels, the macroscopic and the microscopic one. On the macroscopic level, the model is analyzed as if it consisted of a homogeneous material with nonlinear behavior, using a standard Newton–Raphson iterative procedure. The nested solution scheme dictates that material properties at the macroscopic level are not calculated using a constitutive law, but by solving an appropriate boundary value problem at the microscopic level, using a homogenization technique. The steps of the method can be summarized as follows: The macroscopic structure is discretized and an appropriate RVE is chosen to represent the microstructure, which is subsequently discretized as well. For the first step of the Newton–Raphson algorithm, zero displacements are assigned to all the nodes of the macrostructure. The macroscopic nodal displacements are used to calculate the macroscopic strain $\bar{\varepsilon}$ at every Gauss Point, using the macroscopic shape function derivatives $\bar{B}$. Next, the macroscopic strain is used to apply appropriate boundary displacements to every RVE, according to the localization rule of the homogenization scheme. After the solution of the resulting boundary value problem, the macroscopic stress $\bar{\sigma}$ and the macroscopic tangent modulus $\bar{\mathbb{C}}$ at every macroscopic Gauss Point are calculated according to the homogenization rule of the homogenization scheme. These are then used to calculate the internal

nodal force vector $\bar{Q}$ and tangential stiffness matrix $\bar{K}$ of the macroscopic structure. If the internal nodal force vector is in equilibrium with the external one, the procedure is terminated. Else, the macroscopic nodal displacements are updated according to the Newton–Raphson algorithm and the procedure is repeated, until convergence is achieved. A typical Newton–Raphson iteration step is illustrated in the flowchart of Fig. 6.

4. Numerical applications

4.1. Model configuration and solution strategy overview

The material analyzed was a polymer matrix reinforced with straight, unidirectional CNTs. Both the matrix and the CNTs were considered linearly elastic. The matrix was composed of polyether-ether-ketone (PEEK), whose elastic modulus and Poisson's ratio were calculated from physical experiments as $E_m = 2.79$ GPa, and $v_m = 0.4$ respectively [2]. The nanotubes were single-walled, with a nominal outer diameter of 14 nm, and their chirality was type armchair (100,100).

First, a small portion of a nanotube was modeled as a space frame, using mMSM. The resulting model was then projected on an EBE with a pipe profile section whose wall thickness was chosen as $t_f = 0.34$ nm. The EBE's mean equivalent diameter and Young's modulus were then calculated from the axial and transverse loading's load–deflection relations of Eq. (1) as $d_{eq,f} = 13.453$ nm and $E_f = 1.051$ TPa respectively [2].

Next, a RVE was modeled, which consisted of a single CNT embedded in a rectangular PEEK matrix. The RVE finite element model is depicted in Fig. 7; the matrix was discretized with plane stress finite elements and the CNT with truss elements, having the properties of the previously derived EBE. Several CNT weight fractions were considered, ranging from 0.1 to 2 per cent, which were obtained by varying the matrix thickness. The CNT-PEEK interaction was modeled using the bond–slip model of Section 3.1.1.1. The constitutive relation of interfacial shear stress was a bilinear one, representing a stick–slip behavior. As shown in Fig. 8, the slope of the first branch of the bilinear curve was equal to $k_E = 10$ GPa/nm, and that of the second branch was equal to $k_T = 1e - 5$ GPa/nm. Various values of ISS, ranging from zero (neat CNT) to infinity (full bond) were considered.

4.2. Microscopic testing

For the microscopic testing, a homogenization scheme pertaining to linear boundary displacements was applied to the previously described RVE finite element model. More specifically, a macroscopic strain in the form $\bar{\varepsilon} = [\bar{\varepsilon}_{11} \quad \bar{\varepsilon}_{22} \quad 2\bar{\varepsilon}_{12}]^T = [\varepsilon_1 \quad -0.4\varepsilon_1 \quad 0]^T$ was applied to the RVE, simulating uniaxial stress loading. The RVE was subjected to strains corresponding to one full cycle of ε_1, ranging between $-\bar{\varepsilon}_{max}$ and $\bar{\varepsilon}_{max}$ ($\bar{\varepsilon}_{max} > 0$), and homogenized stress–strain curves were obtained for a strain amplitude ($\bar{\varepsilon}_{max}$) range between one and 15 percent and CNT weight fractions equal to 0.1, 0.5, 1, 1.5 and 2 per cent.

The damping ratio ξ of the homogenized material was then calculated for each stress–strain curve as:

$$\xi = \frac{A_{micro}}{2\pi\bar{\sigma}_{max}\bar{\varepsilon}_{max}} \qquad (25)$$

where A_{micro} denotes the area of the homogenized stress–strain loop, $\bar{\varepsilon}_{max}$ denotes the amplitude of the applied homogenized strain $\bar{\varepsilon}_{11}$ and $\bar{\sigma}_{max}$ denotes the homogenized stress $\bar{\sigma}_{11}$ corresponding to $\bar{\varepsilon}_{max}$.

Fig. 9 displays the homogenized stress $\bar{\sigma}_{11}$ as a function of the applied homogenized strain $\bar{\varepsilon}_{11}$ for CNT weight fraction equal to
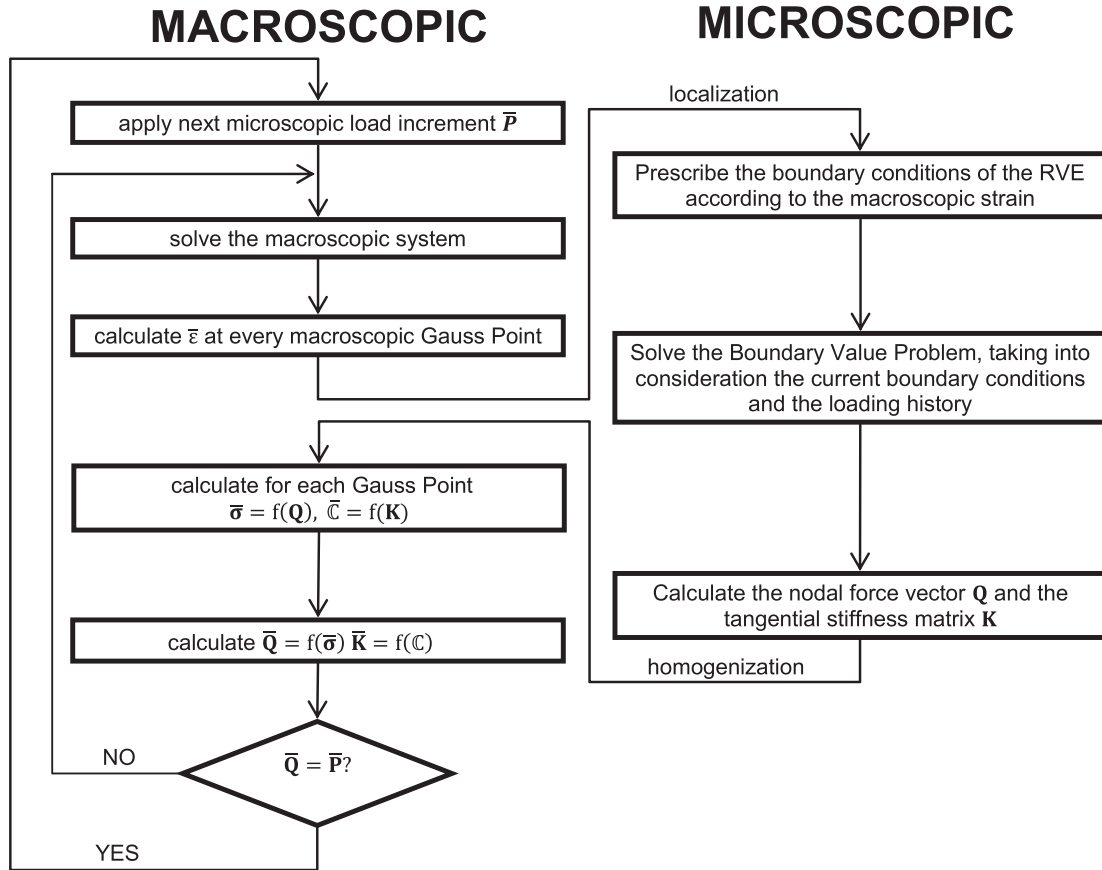
MACROSCOPIC

apply next microscopic load increment $\overline{P}$

solve the macroscopic system

calculate $\bar{\varepsilon}$ at every macroscopic Gauss Point

calculate for each Gauss Point
$\overline{\sigma} = f(\mathbf{Q}), \; \overline{\mathbb{C}} = f(\mathbf{K})$

calculate $\overline{\mathbf{Q}} = f(\overline{\sigma}) \; \overline{\mathbf{K}} = f(\mathbb{C})$

NO $\overline{\mathbf{Q}} = \overline{\mathbf{P}}?$

YES

MICROSCOPIC

localization

Prescribe the boundary conditions of the RVE according to the macroscopic strain

Solve the Boundary Value Problem, taking into consideration the current boundary conditions and the loading history

Calculate the nodal force vector $\mathbf{Q}$ and the tangential stiffness matrix $\mathbf{K}$

homogenization

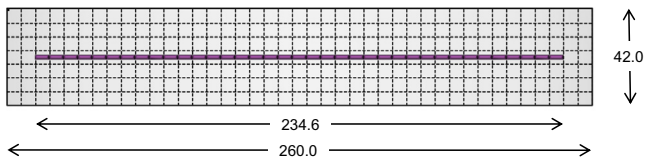**Fig. 6.** The algorithm for a typical Newton–Raphson step of the nested solution scheme.

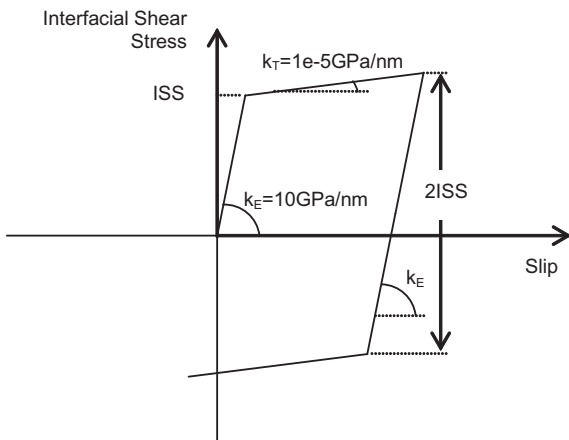**Fig. 7.** The microscopic discretized model. The CNT is indicated with purple. Dimensions are in nm.

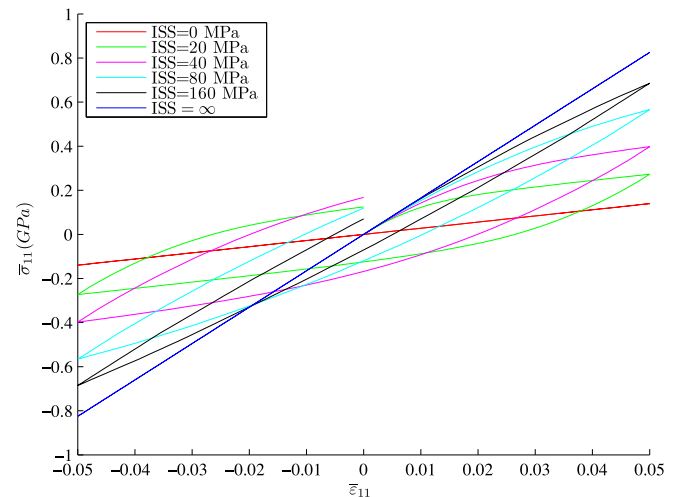**Fig. 8.** Variation of interfacial shear stress with respect to slippage.

Fig. 9. Variation of the homogenized stress $\bar{\sigma}_{11}$ with respect to the applied strain $\bar{\varepsilon}_{11}$ for weight fraction equal to $w_f = 1\%$ and strain amplitude equal to $\bar{\varepsilon}_{max} = 5\%$.

$w_f = 1\%$, various values of ISS and strain amplitude equal to $\bar{\varepsilon}_{max} = 5\%$. Observing Fig. 9, two extreme cases can be discerned: (1) ISS = 0: There is no stress transfer mechanism between the CNT and the polymer. In this case, the properties of the homogenized RVE coincide with those of the polymer. (2) ISS = ∞: In this case full bond exists between the CNT and the polymer. In both cases, the homogenized RVE displays linearly elastic behavior.

Between those extremes, the RVE displays hysteretic behavior. This behavior is better captured in Fig. 10a–c, which depict the variation of the damping ratio ξ with respect to ISS for various weight fractions and strain amplitude equal to 3%, 5% and 10% respectively. Observing this figure, it is obvious that larger weight fractions yield larger damping ratio coefficients for smaller ISS values. This observation however does not hold for larger ISS values. Each curve displays a peak (ξ_{max}), which is shifted to lower ISS values for larger

weight fractions. The peak of each curve corresponds to ISS values for which the CNT has fully slipped when the applied strain is equal to the strain amplitude; if the CNT has slipped earlier or if it hasn't slipped in its entirety at the RVE's most strained state, the damping ratio is lower than the peak value (ξ_{max}).

Observing Fig. 10, it is also worth noting that for different strain amplitudes, the peak value of the damping ratio for a certain weight fraction does not change; it is simply shifted to a different ISS value. In other words, for a certain weight fraction and ISS value, there exists a strain amplitude for which the damping ratio reaches its maximum value, which, for the weight fraction in question is constant and independent of the value of ISS. This is shown clearly in Fig. 11, which depicts the damping ratio ξ as a function of $\bar{\varepsilon}_{max}$ for various ISS values. That is, the "damping potential" of the
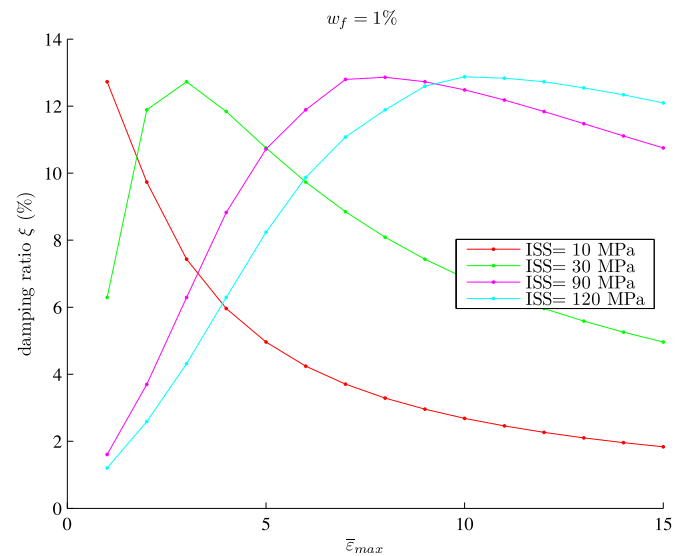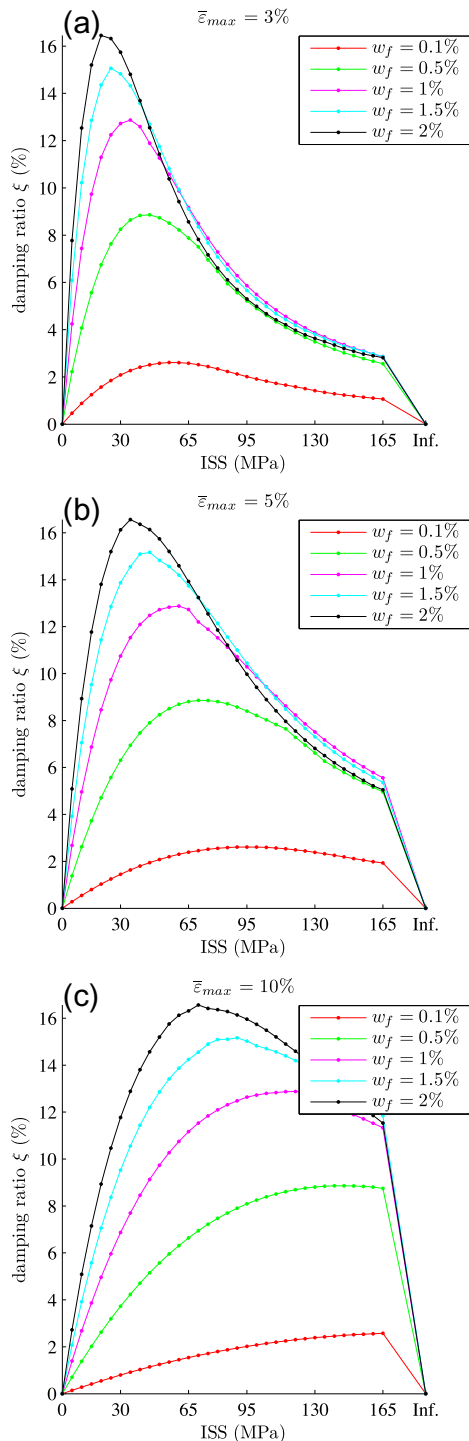

Fig. 10. Variation of the damping ratio ξ with respect to ISS for various weight fractions and strain amplitude equal to (a) $\bar{\varepsilon}_{max} = 3\%$, (b) $\bar{\varepsilon}_{max} = 5\%$ and (c) $\bar{\varepsilon}_{max} = 10\%$.

Fig. 11. Variation of the damping ratio ξ with respect to the strain amplitude $\bar{\varepsilon}_{max}$ for various values of ISS and weight fraction equal to 1%.
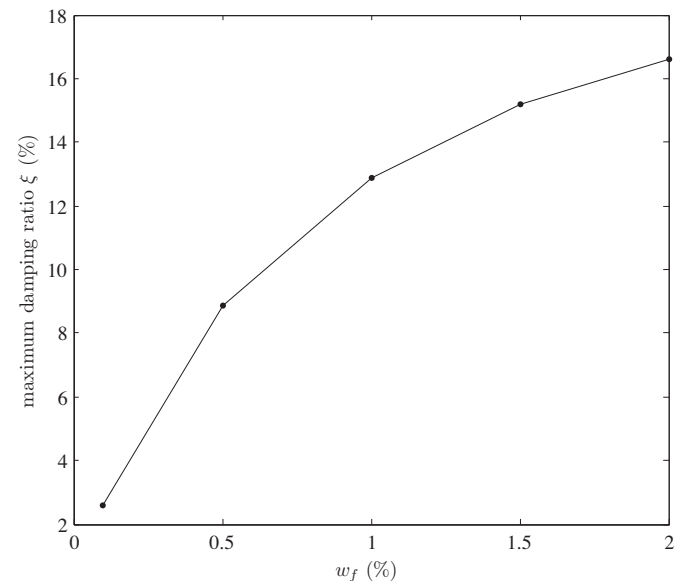

Fig. 12. Variation of the maximum damping ratio (for all strain amplitudes and ISS values) with respect to the weight fraction.

material is independent of the value of ISS and of the strain amplitude, and increases for higher weight fractions. This result is summarized in Fig. 12, which displays the increase of ξ_{max} as a function of w_f. This behavior can be attributed to the adopted interfacial constitutive law of Fig. 8. The slope of both lines of this bilinear
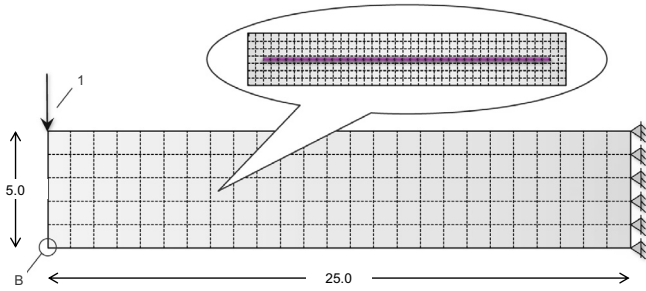

Fig. 13. The macroscopic model configuration. The thickness of the structure is equal to 1. The units are GN, m.

curve which describes the interfacial shear stress as a function of slippage does not change for different ISS values. Hence, the stress–strain loops which correspond to the maximum damping ratio for a certain weight fraction are similar, and their size is proportional to the value of ISS; therefore, the maximum damping ratio is exactly the same for all values of ISS. Moreover, the strain amplitude for which the damping ratio is maximized is proportional to the value of ISS.

4.3. Macroscopic testing

In order to investigate the impact of ISS and CNT weight fraction on the overall behavior of macroscopic structures consisting of CNT-reinforced polymer, the cantilever beam of Fig. 13 was selected and loaded with a vertical load of a unit magnitude (in GN), scaled by a loading factor λ. The beam was modeled using plane stress elements, and was analyzed using the nested (FE^2) solution scheme, as described in Section 3.2. Various CNT weight fractions, equal to 0.1, 0.5, 1, 1.5 and 2 per cent were considered, while ISS was taken equal to $10, 40, 80$ and 160 MPa. One full cycle
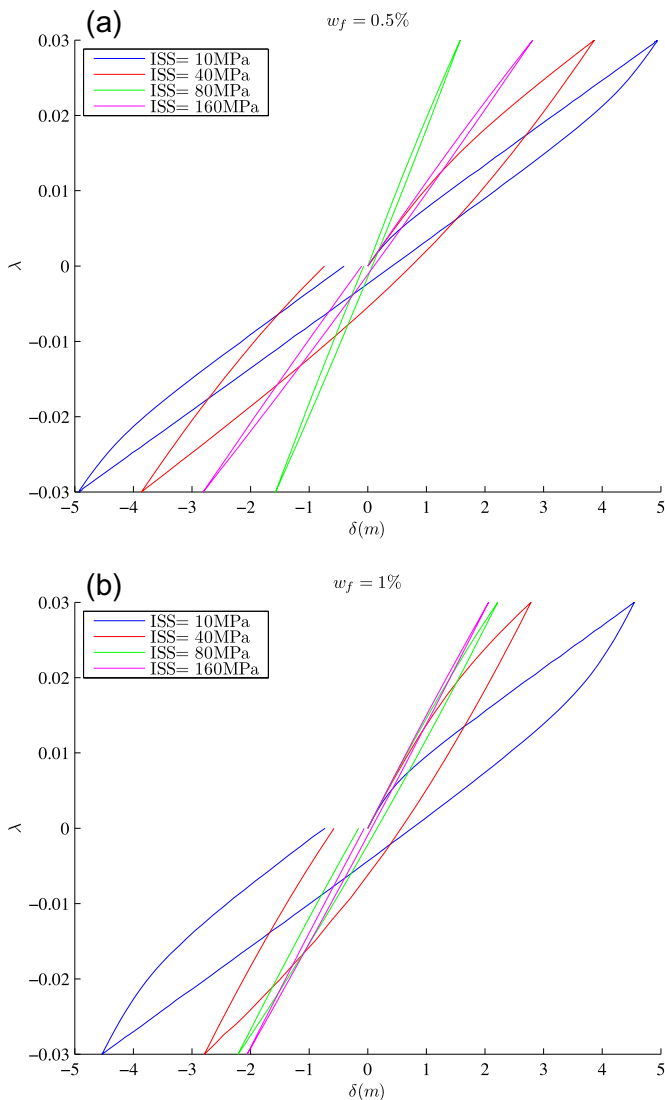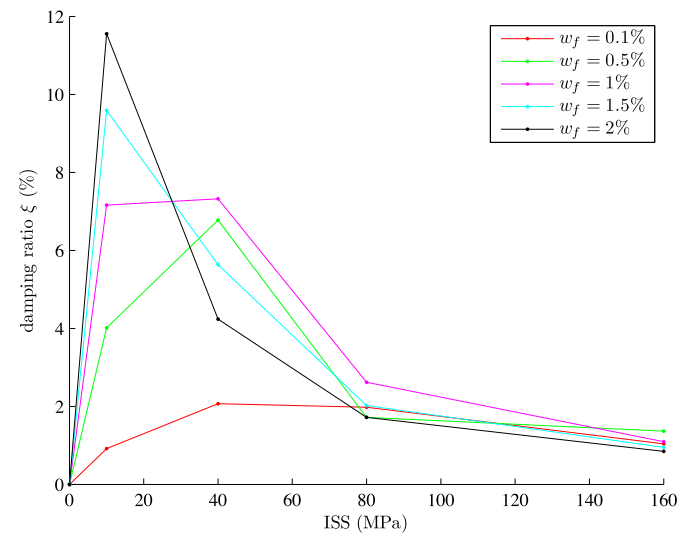

Fig. 15. Variation of the damping ratio ξ of the macroscopic model with respect to ISS for weight fraction equal to $0.1, 0.5, 1$ and 2 percent.

Fig. 14. Force–displacement curves of the macroscopic model for two weight fractions ((a):0.5% and (b):1%) and various values of ISS.
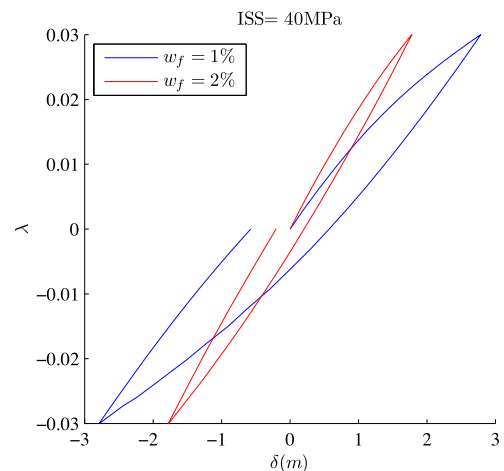

Fig. 16. Force–displacement curves of the macroscopic model for ISS equal to 40 MPa and weight fraction equal to 1 and 2 percent.
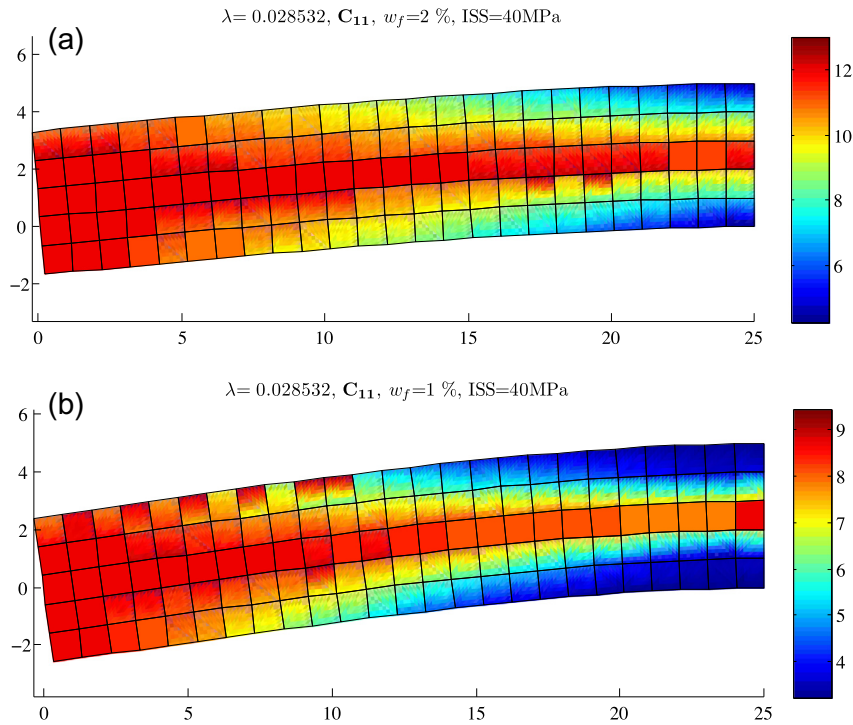
Fig. 17. Spatial distribution of the $\bar{\mathbb{C}}_{11}$ coefficient for two weight fractions ((a):2% and (b):1%) and ISS = 40 MPa, $\lambda = 0.028532$. $\bar{\mathbb{C}}_{11}$ is a good measure of microstructural slippage, as lower values (which are indicated with cooler tones in the diagram) correspond to a higher amount of microstructural slippage.

of the load was applied, for values of the loading factor λ between 0.03 and −0.03. In order to obtain force–displacement curves of the structure, the vertical displacement δ at point B was monitored. Subsequently, the damping ratio of the structure for the loading in question was calculated from the $\lambda - \delta$ curve as:

$$\xi = \frac{A_{\text{macro}}}{2\pi\lambda_{max}\delta_{max}} \tag{26}$$

where A_{macro} denotes again the area of the force–displacement loop, λ_{max} denotes the amplitude of the applied force, which is equal to 0.03, and δ_{max} denotes the vertical displacement of point B corresponding to λ_{max}.

Fig. 14a and b display the force–displacement curves of the structure for various ISS values and weight fractions equal to 0.5 and 1 percent respectively. As was the case for the microscopic experiment, higher ISS values lead to a stiffer structure for a certain weight fraction. Moreover, as ISS increases, the hysteresis loops of the structure increase in size until a critical ISS value (ISS$_{\text{crit}}$). The hysteretic behavior of the structure is better described in Fig. 15, which shows the damping ratio ξ with respect to the variation of ISS for several weight fractions. Comparing Fig. 15 with Fig. 10, it is obvious that the results of the macroscopic experiment are similar to those obtained from the microscopic experiment. For every weight fraction there exists a critical ISS value (ISS$_{\text{crit}}$) for which the damping ratio ξ reaches its maximum value ξ_{max}. For ISS = ISS$_{\text{crit}}$, a fairly large area of the macroscopic structure has experienced full microstructural slippage at its most deformed state. For a certain weight fraction, slipped areas larger (for ISS $<$ *ISS*$_{\text{crit}}$) or smaller (for ISS $>$ ISS$_{\text{crit}}$) than the critical one lead to ξ values lower than ξ_{max}. Moreover, for larger weight fractions the peak of the damping ratio is shifted to smaller ISS values, as was the case for the microscopic experiment as well. It should also be noted that larger weight fractions do not necessarily lead to higher damping ratios. More

specifically, for small values of ISS (less than ISS$_{\text{crit}}$) larger weight fractions result in higher damping ratios; this does not hold, however, for values of ISS larger than ISS$_{\text{crit}}$. Inspection of Fig. 15 reveals that for the larger weight fraction ($w_f = 2\%$), the value of ξ drops steeply for ISS values larger than ISS$_{\text{crit}}$. In Fig. 16 it is demonstrated that for ISS = 40 MPa, the damping ratio corresponding to $w_f = 2\%$ is almost half of the one corresponding to $w_f = 1\%$, which is reflected on the large difference in size of the hysteresis loops for both cases. This result is further demonstrated in the overall damping behavior of the macrostructure, which is displayed in Fig. 17a and b, which plot the spatial distribution of the $\mathbb{C}_{11}$ term of the macroscopic tangent modulus $\bar{\mathbb{C}}$ of Eq. (12) for weight fractions equal to 2% and 1% respectively. From these figures it is obvious that for the higher weight fraction, the areas for which full microstructural slippage has occurred (indicated with blue) are much smaller than those corresponding to the lower weight fraction. Consequently, the cumulative amount of energy dissipated in the case of the lower weight fraction is much larger, which leads to a higher damping ratio. Finally, it is worth noting that the maximum damping ratio achieved for the uniaxial stress conditions of the microscopic experiment (approximately 16%) is higher than the one achieved for the bending loading of the macroscopic experiment (12%).

5. Conclusions

In this work, a CNT-reinforced polymer was studied and a cantilever beam consisting of this material was analyzed using a multiscale strategy based on a combination of a sequential and a semiconcurrent (FE^2) approach; for the FE^2, a homogenization scheme pertaining to linear displacement boundary conditions was used. The polymer examined was PEEK, reinforced with straight unidirectional SWCNTs; both materials were considered to be linearly

elastic. For the microstructural description at the RVE level, CNT-polymer interaction was modeled using a bond–slip model in which the interfacial slippage was described with a stick–slip model. A cantilever beam consisting of the SWCNT-reinforced PEEK was considered as the macroscopic example, which was subjected to cyclic load at the free edge.

The results of the sensitivity analysis regarding the effect of ISS and CNT weight fraction on the stiffness of CNT-reinforced composites revealed that higher values of CNT weight fraction and ISS increase the stiffness of the end product significantly. On the other hand, in order to improve the damping properties of a structure, an optimum extent of microstructural slippage has to be achieved. Higher weight fractions can yield larger damping ratios if ISS is low enough to achieve an optimum extent of microstructural slippage. It should be noted that the value of ISS which maximizes the damping ratio for a certain weight fraction is loading-specific. In general, increasing the amplitude of the applied load increases the ISS for which the damping ratio is maximized. Moreover, the value of damping ratio that can be achieved for a certain structure depends on the way the structure is loaded. For the cantilever beam which was studied under a bending load, the values of damping ratio that were achieved were significantly lower than those of the uniaxial strain test.

Clearly, the effect of the interface on the behavior of macroscopic structures is critical and is worth further examination. Moreover, CNTs have been shown to be particularly susceptible to P-Δ effects, owing to their very large length in relation to their diameter; consequently, it would be of interest to investigate how the damping mechanism due to slippage is influenced by second order phenomena regarding the behavior of CNTs. All these aspects will be incorporated in future research by the authors.

Acknowledgments

Appendix A. Supplementary data

Supplementary data associated with this article can be found, in the online version, at http://dx.doi.org/10.1016/j.compstruct.2015.10.025.

References

[1] Thostenson ET, Ren Z, Chou T-W. Advances in the science and technology of carbon nanotubes and their composites: a review. Compos Sci Technol 2001;61:1899–912. http://dx.doi.org/10.1016/S0266-3538(01)00094-X.

[2] Savvas DN, Papadopoulos V, Papadrakakis M. The effect of interfacial shear strength on damping behavior of carbon nanotube reinforced composites. Int J Solids Struct 2012;49:3823–37. http://dx.doi.org/10.1016/j.ijsolstr.2012.08.031.

[3] Ajayan PM, Suhr J, Koratkar N. Utilizing interfaces in carbon nanotube reinforced polymer composites for structural damping. J Mater Sci 2006;41:7824–9. http://dx.doi.org/10.1007/s10853-006-0693-4.

[4] Zhou X, Shin E, Wang KW, Bakis CE. Interfacial damping characteristics of carbon nanotube-based composites. Compos Sci Technol 2004;64:2425–37. http://dx.doi.org/10.1016/j.compscitech.2004.06.001.

[5] Montinaro N, Pantano A. Parameters influencing the stiffness of composites reinforced by carbon nanotubes – A numerical–analytical approach. Compos Struct 2014;109:246–52. http://dx.doi.org/10.1016/j.compstruct.2013.11.004.

[6] Nafar Dastgerdi J, Marquis G, Salimi M. Micromechanical modeling of nanocomposites considering debonding and waviness of reinforcements. Compos Struct 2014;110:1–6. http://dx.doi.org/10.1016/j.compstruct.2013.11.017.

[7] Ayatollahi MR, Shadlou S, Shokrieh MM. Multiscale modeling for mechanical properties of carbon nanotube reinforced nanocomposites subjected to different types of loading. Compos Struct 2011;93:2250–9. http://dx.doi.org/10.1016/j.compstruct.2011.03.013.

[8] Rahmat M, Hubert P. Carbon nanotube–polymer interactions in nanocomposites: a review. Compos Sci Technol 2011;72:72–84. http://dx.doi.org/10.1016/j.compscitech.2011.10.002.

[9] Pan Y, Weng GJ, Meguid SA, Bao WS, Zhu ZH, Hamouda AMS. Interface effects on the viscoelastic characteristics of carbon nanotube polymer matrix composites. Mech Mater 2013;58:1–11. http://dx.doi.org/10.1016/j.mechmat.2012.10.015.

[10] Kao CC, Young RJ. Modeling the stress transfer between carbon nanotubes and a polymer matrix during cyclic deformation. In: IUTAM Symp. Model. Nanomater. Nanosyst.. Springer Science+Business Media B.V.; 2009. p. 211–20.

[11] Kao CC, Young RJ. Assessment of interface damage during the deformation of carbon nanotube composites. J Mater Sci 2010;45:1425–31. http://dx.doi.org/10.1007/s10853-009-3947-0.

[12] Barber AH, Cohen SR, Eitan A, Schadler LS, Wagner HD. Fracture transitions at a carbon-nanotube/polymer interface. Adv Mater 2006;18:83–7. http://dx.doi.org/10.1002/adma.200501033.

[13] Wagner HD, Vaia RA. Nanocomposites: issues at the interface. Mater Today 2004;7:38–42. http://dx.doi.org/10.1016/S1369-7021(04)00507-3.

[14] Desai AV, Haque MA. Mechanics of the interface for carbon nanotube-polymer composites. Thin-Walled Struct 2005;43:1787–803. http://dx.doi.org/10.1016/j.tws.2005.07.003.

[15] Jiang LY, Huang Y, Jiang H, Ravichandran G, Gao H, Hwang KC, et al. A cohesive law for carbon nanotube/polymer interfaces based on the van der Waals force. J Mech Phys Solids 2006;54:2436–52. http://dx.doi.org/10.1016/j.jmps.2006.04.009.

[16] Ganesan Y, Peng C, Lu Y, Loya PE, Moloney P, Barrera E, et al. Interface toughness of carbon nanotube reinforced epoxy composites. ACS Appl Mater Interfaces 2011;3:129–34. http://dx.doi.org/10.1021/am1011047.

[17] Wong M, Paramsothy M, Xu XJ, Ren Y, Li S, Liao K. Physical interactions at carbon nanotube-polymer interface. Polymer (Guildf) 2003;44:7757–64. http://dx.doi.org/10.1016/j.polymer.2003.10.011.

[18] Lachman N, Daniel Wagner H. Correlation between interfacial molecular structure and mechanics in CNT/epoxy nano-composites. Compos Part A Appl Sci Manuf 2010;41:1093–8. http://dx.doi.org/10.1016/j.compositesa.2009.08.023.

[19] Mu M, Osswald S, Gogotsi Y, Winey KI. An in situ Raman spectroscopy study of stress transfer between carbon nanotubes and polymer. Nanotechnology 2009;20:335703. http://dx.doi.org/10.1088/0957-4484/20/33/335703.

[20] Chowdhury SC, Okabe T. Computer simulation of carbon nanotube pull-out from polymer by the molecular dynamics method. Compos Part A Appl Sci Manuf 2007;38:747–54. http://dx.doi.org/10.1016/j.compositesa.2006.09.011.

[21] Suhr J, Koratkar N, Keblinski P, Ajayan P. Viscoelasticity in carbon nanotube composites. Nat Mater 2005;4:134–7. http://dx.doi.org/10.1038/nmat1293.

[22] Li Y, Seidel GD. Multiscale modeling of the effects of nanoscale load transfer on the effective elastic properties of unfunctionalized carbon nanotube–polyethylene nanocomposites. Model Simul Mater Sci Eng 2014;22:25023. http://dx.doi.org/10.1088/0965-0393/22/2/025023.

[23] Wernik JM, Cornwell-Mott BJ, Meguid SA. Determination of the interfacial properties of carbon nanotube reinforced polymer composites using atomistic-based continuum model. Int J Solids Struct 2012;49:1852–63. http://dx.doi.org/10.1016/j.ijsolstr.2012.03.024.

[24] Barber AH, Cohen SR, Kenig S, Wagner HD. Interfacial fracture energy measurements for multi-walled carbon nanotubes pulled from a polymer matrix. Compos Sci Technol 2004;64:2283–9. http://dx.doi.org/10.1016/j.compscitech.2004.01.023.

[25] Coto B, Antia I, Barriga J, Blanco M, Sarasua JR. Influence of the geometrical properties of the carbon nanotubes on the interfacial behavior of epoxy/CNT composites: a molecular modelling approach. Comput Mater Sci 2013;79:99–104. http://dx.doi.org/10.1016/j.commatsci.2013.05.057.

[26] Wagner HD, Lourie O, Feldman Y, Tenne R. Stress-induced fragmentation of multiwall carbon nanotubes in a polymer matrix. Appl Phys Lett 1998;72:188–90. http://dx.doi.org/10.1063/1.120680.

[27] Frankland SJV, Harik VM. Analysis of carbon nanotube pull-out from a polymer matrix. Surf Sci 2003;525:L103–8. http://dx.doi.org/10.1016/S0039-6028(02)02532-3.

[28] Tsuda T, Ogasawara T, Deng F, Takeda N. Direct measurements of interfacial shear strength of multi-walled carbon nanotube/PEEK composite using a nano-pullout method. Compos Sci Technol 2011;71:1295–300. http://dx.doi.org/10.1016/j.compscitech.2011.04.014.

[29] Gou J, Minaie B, Wang B, Liang Z, Zhang C. Computational and experimental study of interfacial bonding of single-walled nanotube reinforced composites. Comput Mater Sci 2004;31:225–36. http://dx.doi.org/10.1016/j.commatsci.2004.03.002.

[30] Li Y, Liu Y, Peng X, Yan C, Liu S, Hu N. Pull-out simulations on interfacial properties of carbon nanotube-reinforced polymer nanocomposites. Comput Mater Sci 2011;50:1854–60. http://dx.doi.org/10.1016/j.commatsci.2011.01.029.

[31] Savvas DN, Papadopoulos V. Nonlinear multiscale homogenization of carbon nanotube reinforced composites with interfacial slippage. Int J Multiscale Comput Eng 2014;2014(12):271–89. http://dx.doi.org/10.1615/IntJMultiComp Eng.007258.

[32] Chen W-H, Cheng H-C, Liu Y-L. Radial mechanical properties of single-walled carbon nanotubes using modified molecular structure mechanics. Comput Mater Sci 2010;47:985–93. http://dx.doi.org/10.1016/j.commatsci.2009.11.034.

[33] Lykidis GC, Spiliopoulos KV. 3D solid finite-element analysis of cyclically loaded RC structures allowing embedded reinforcement slippage. J Struct Eng 2008;134:629–38. http://dx.doi.org/10.1061/(ASCE)0733-9445(2008)134:4(629).

[34] Miehe C, Koch A. Computational micro-to-macro transitions of discretized microstructures undergoing small strains. Arch Appl Mech 2002;72:300–17. http://dx.doi.org/10.1007/s00419-002-0212-2.

[35] Feyel F. A multilevel finite element method (FE2) to describe the response of highly non-linear structures using generalized continua. Comput Methods Appl Mech Eng 2003;192:3233–44. http://dx.doi.org/10.1016/S0045-7825(03)00348-7.